Extremely Stable Platinum-Amorphous Carbon Electrocatalyst within Hollow Graphitized Carbon Nanofibers for the Oxygen Reduction Reaction

Maria del Carmen Gimenez-Lopez, Abdullah Kurtoglu, Darren A. Walsh, and Andrei N. Khlobystov**

One of the biggest challenges facing the world today is the increasing global demand for affordable and secure energy, while at the same time tackling climate change. The proton exchange membrane fuel cells (PEMFC) is a very promising new technology for clean and renewable energy.[1–4] However, the stability of platinum (Pt)-based catalysts is one of the most important issues which must be solved in order to make PEMFC a viable alternative to traditional energy technologies.

Porous carbon materials are the most widely studied electrocatalyst supports, as they combine large surface area with a high electrical conductivity.[5] Highly graphitized carbon materials such as carbon nanotubes have been put forward due to their unique corrosion resistance.[6,7] However, the chemical inertness of the perfect basal plane of a multi-walled carbon nanotube (MWNT) results in low dispersion and facile agglomeration of platinum nanoparticles (PtNP) after potential cycling,[8–11] leading to a rapid decrease of the electrochemical surface area (ECSA) and activity that detrimentally affect the catalyst durability.

To overcome the above stability problems of intrinsically metastable PtNP electrocatalysts, tremendous effort has been made to develop the state-of-the-art of nanohybrid materials often involving a complex methodology for Pt encapsulation or adsorption on the surface of nanocarbons using expensive porous inorganic host-materials, such as tungsten oxide/carbide,[12–15] and tin dioxide[16–18] (which unfortunately show limited electrical conductivity). An excellent example is the work by Sun and co-workers study which reported the effect of the encapsulation of PtNP on the oxygen reduction reaction (ORR) after just 4000 cycles for fuel cell applications in zirconia nanocages using area-selective atomic layer deposition on the external surface of carbon nanotubes.[19] However, the limited scalability and processing of this approach still present a challenge to harnessing the full potential of durability of Pt-nanocatalyst enhanced by confinement.

Unlike concentric MWNT, highly graphitized hollow carbon nanofibers (GNF) exhibit corrugated interior surfaces defined by internal stacked-nanocone structures, with typical step-edge heights of the rolled-up graphene sheets of ≈3 nm (Figure S1, Supporting Information). Recent studies in our group have shown that the corrugated graphitic steps of GNF not only can control positions of NP,[20] but also provide a stabilization mechanism for NP growth.[21,22] We have previously observed that gold NP adsorbed on the internal surfaces of GNF grow to the same maximum size of ≈6 nm, regardless of the stimulus for their growth (i.e., heat or electron beam), as the GNF internal step-edges impose significant barriers for the migration of the metal NPs, precluding their growth by coalescence mechanisms.

In this study, we demonstrate the combined effect of nanoscale confinement and graphitic step-edge stabilization of PtNP in GNF, which have a profound effect on electrocatalytic durability of platinum. We discovered a significantly improved electrochemical stability of PtNP, even after 50 000 cycles of ORR, outperforming that of a commercial state-of-the-art Pt electrocatalyst (Pt/C) used as a benchmark in our study. High-resolution transmission electron microscopy (HRTEM) imaging employed to investigate structural changes in PtNP inserted in shortened GNF (PtNP@S-GNF) under electrocatalytic conditions reveals a surprising new mechanism of the PtNP stabilization which sheds light on the fundamental nanoscale phenomena underpinning the superior electrocatalytic stability observed in the ORR. A significantly simplified, scalable approach for the stabilization of PtNP catalytic centers opens a new methodology for construction of hybrid electrocatalyst nanomaterial (PtNP@S-GNF) where metal NPs are confined and simultaneously electrically connected to the electrode, retaining 88% of their activity after 50 000 reaction cycles, which can enable the sustainable use of platinum for fuel cell applications.

PtNPs with average diameter of ≈3 nm (Figures S2 and S3, Supporting Information) have been synthesized using a well-established protocol based on the reduction of platinum (II) acetylacetonate ($Pt(acac)_2$) at elevated temperatures (200 °C) in the presence of surfactant molecules.[23] Free-standing PtNP have been encapsulated by capillary forces from a hexane solution into the hollow GNF, opened and shortened by mechanical milling to 0.2–20 μm length (S-GNF) prior to

Dr. M. del Carmen Gimenez-Lopez, A. Kurtoglu, Dr. D. A. Walsh, Prof. A. N. Khlobystov
School of Chemistry
University of Nottingham
University Park
Nottingham NG7 2RD, UK
E-mail: maria.gimenez-lopez@nottingham.ac.uk; andrei.khlobystov@nottingham.ac.uk
Prof. A. N. Khlobystov
Nanoscale & Microscale Research Centre
University of Nottingham
University Park
Nottingham NG7 2RD, UK

DOI: 10.1002/adma.201602485

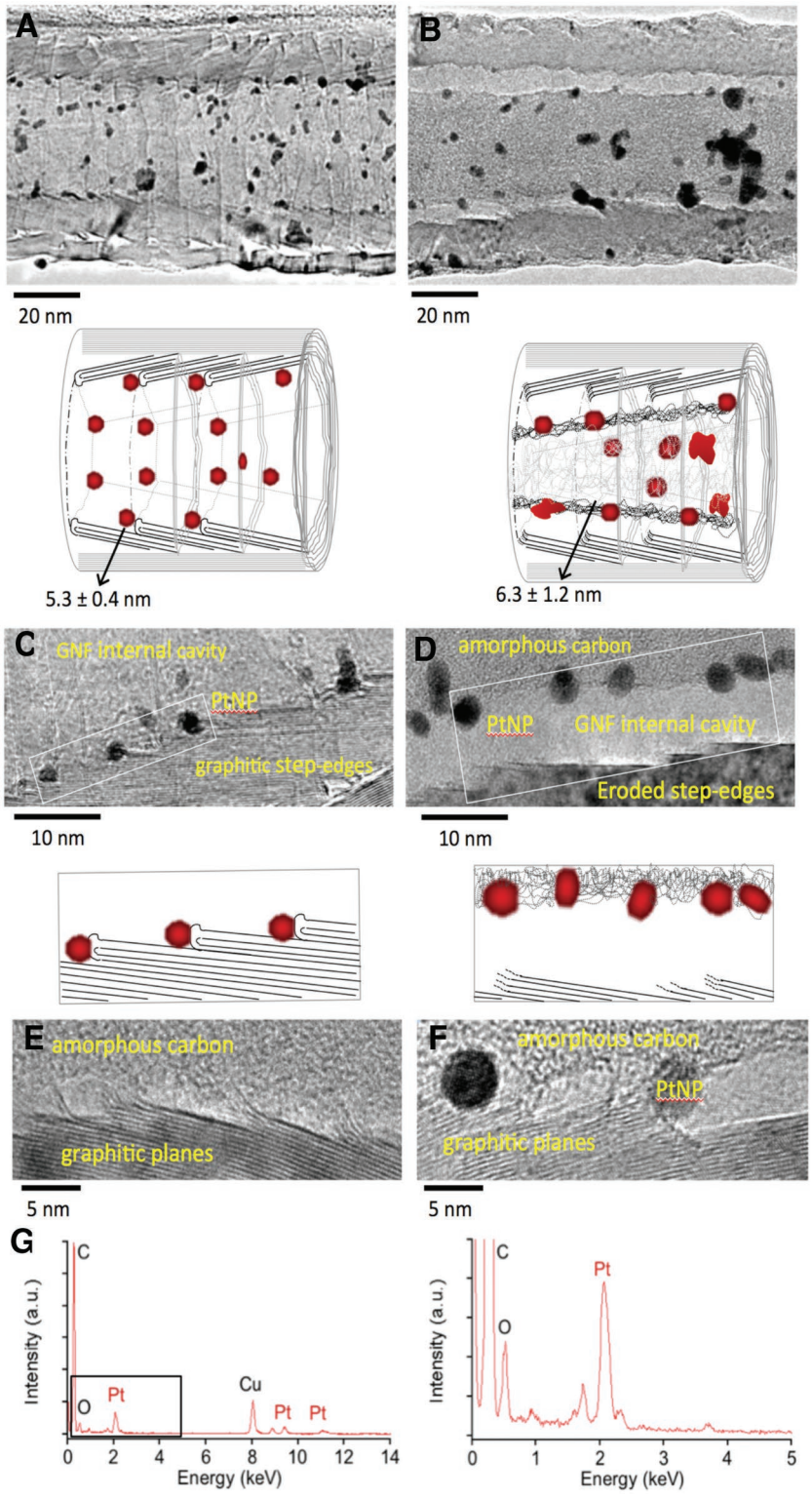

Figure 1. HRTEM images of PtNP@S-GNF before oxygen reduction reaction A) with PtNP positioned predominantly at the graphitic step-edges and C) the internal cavity of GNF completely free of NP (step-edges running across the GNF are clearly visible as transverse lines in the image). After exposure of PtNP@S-GNF to 50 000 potential cycles in ORR, B) internal cavity of GNF becomes filled with amorphous carbon located in the middle of the GNF, D) with all PtNP adhered to the amorphous carbon. Graphitic step-edges appear to be "unravelling" during the ORR giving rise to amorphous carbon, as clearly indicated by E) individual graphitic layers of GNF observed half-way through amorphization. PtNP after 50 000 potential cycles remain inside GNF D) adhered to amorphous carbon or F) sandwiched between the amorphous carbon and GNF wall. In either case, a 5–10 nm gap formed between the inner wall of GNF and the layer of amorphous carbon allowing efficient access of reactants to catalytic centers PtNP during ORR. Energy dispersive X-ray analysis confirms that composition of PtNP@S-GNF remains virtually unchanged after 50 000 cycles, and local-probe EDX analysis shows ≈1.5 at % of oxygen incorporated in the amorphous carbon structure (G).

insertion of PtNP. In contrast to the smooth graphitic exterior surfaces of S-GNF, the graphitic step-edges in the interiors of S-GNF provide sites for strong interaction between the host S-GNF and the guest PtNP through van der Waals forces. When NP is of a size commensurate with the height of the step-edge (≈3 nm), as in the case of our PtNP, this interaction is so strong that once the PtNP are anchored to the step-edges they cannot be dislodged. The corrugated interior and atomically smooth exterior of S-GNF drive the effective transport and encapsulation of PtNP into S-GNF, whereas PtNP adsorbed on the S-GNF exteriors can be removed by sonication in an organic solvent. The resulting hybrid material was carefully washed with hexane after sonication to eliminate any PtNP absorbed on the external surface of S-GNF followed by heating in air at 175 °C for 5 h which facilitates the removal of the organic surfactant molecules from PtNP, as confirmed by thermogravimetric analysis (TGA) (Figure S4, Supporting Information). The thus-formed PtNP@S-GNF electrocatalyst consists of surfactant-free PtNP ripened to a uniform size of ≈5.3 ± 0.4 nm that remain immobilized at the graphitic step-edges of GNF (**Figure 1**A,C, and Figures S5 and S6, Supporting Information). The growth of the encapsulated PtNP, and thus their aggregation above ≈6 nm, is prevented not only by structural factors (i.e., the nanocone step-edges),[21] but also by the effects of electrostatic interaction (i.e., electron transfer from the nanocone graphene stack).[22] While TGA analysis showed the platinum loading in PtNP@S-GNF was around 10% by weight, TEM imaging combined with energy-dispersive X-ray (EDX) analysis performed on this hybrid material showed that the vast majority of the PtNP are positioned within S-GNF cavities, as demonstrated by specimen titling experiments in TEM. The uniform distribution of PtNP within S-GNF cavities combined with NP diameters closely matching

Adv. Mater. **2016**,
DOI: 10.1002/adma.201602485

the height of graphitic step-edges are expected to maximize the electrochemical contact between the PtNP and the electrode and to hinder PtNP migration and coalescence during electrocatalysis.

The electrochemical performance of the PtNP@S-GNF was studied at room temperature in a nitrogen-saturated 0.1 M $HClO_4$ by cyclic voltammetry (CV), and compared with that of a commercial platinum on carbon black (Pt/C, NP diameter: 3.3 ± 0.7 nm) (Figure S7, Supporting Information) with the same Pt loading (14 µg cm^{-2} loading) under exactly the same conditions. Electrocatalyst stability studies involving 50 000 cycles were performed in an accelerated stability test by continuously applying linear potential sweeps from 0.6 to 1.1 V, which caused surface oxidation/reduction cycles of platinum. Changes in the electrochemically active Pt surface area and the electrocatalytic activity toward the ORR were carefully determined every 10 000 cycles (**Figure 2**A). Polarization curves for the ORR obtained for both electrocatalyst on a rotating disk electrode in O_2-saturated 0.1 M $HClO_4$ solution at 1600 rpm were also investigated every 10 000 cycles (Figure 2B, and Figure S8, Supporting Information).

The PtNP@S-GNF and the commercial catalyst (Pt/C) showed similar hydrogen desorption and adsorption features in the potential region between 0.05 and 0.30 V, and the onset of the oxide formation in the anodic sweep. However, the initial ECSA for the PtNP@S-GNF is lower than for the commercial Pt/C due to a smaller initial NP size in the latter material (measured by TEM) (Table S1, Supporting Information). The ORR half-wave potential ($E_{1/2}$) for PtNP@S-GNF (0.785 V) is marginally lower than the one found for the commercial catalyst (0.840 V), suggesting that, in principle, the activity of our electrocatalyst material is slightly lower than the commercial Pt/C. This is also in agreement with the difference in specific activity at 0.85 V observed for the commercial Pt/C electrocatalyst (0.544 mA cm^{-2}) and PtNP@S-GNF (0.360 mA cm^{-2}) that was determined by normalizing the kinetic limiting current density (J_k) to the calculated ECSA values (Table S1, Supporting Information). A Tafel analysis of the rotating ring-disk electrode (RRDE) data (E vs $\log(J_k)$) for PtNP@S-GNF and the commercial catalyst after 5000 potential cycles is shown in the Supporting Information (Figure S9, Supporting Information).

While the overall initial performance of Pt on carbon black appears to be better than for PtNP inside GNF, only after the first 5000 cycles the specific activity of PtNP@S-GNF became slightly higher (0.35 mA cm^{-2}) than the specific activity of Pt/C commercial catalyst (0.312 mA cm^{-2}) under same conditions (**Figure 3**A and Table S1, Supporting Information). This clearly indicates that the stability of catalytic centers in PtNP@S-GNF is significantly enhanced as compared to the commercial catalyst. Furthermore, TEM analysis of both electrocatalysts after 5000 cycles provides explanation for the observed performance as no significant changes in particle size was found for PtNP@S-GNF (an average increase of size ≈0.5 nm) which contrasts to the commercial electrocatalyst Pt/C showing an average increase of PtNP size ≈1.4 nm (from 3.3 to 4.7 nm) (Table S1, Supporting Information). Internal graphitic step-edges of GNF combined with the polygonal cross-section of GNF channels ensure that the surface area of contact between the PtNP and GNF in PtNP@S-GNF is maximized when the PtNP are located at the apexes of the graphitic facets of step-edges (Figure S1, Supporting Information), which leads to a drastic enhancement in the van der Waals interactions between the PtNP and the carbon nanostructure that immobilize the NP, thus precluding their migration and growth beyond 6 nm during electrochemical cycling. In contrast, the ECSA values obtained for Pt/C correlate well with the continuouly increasing NP size in this electrocatalyst during ORR and hence electroactive surface area of platinum that gradually decreases with a growing number of the potential cycles (Figure 3B and Table S1, Supporting Information). The lack of stability of PtNP on carbon black may be related to the absence of long-range order in in this support material leading to electrochemical corrosion that aggravates the PtNP sintering and leads to a reduced durability of Pt/C. The degradation in half-wave potential of ORR polarization curves over the first 5000 cyles for PtNP@S-GNF of only 2 mV, that is in sharp contrast with that observed for the Pt/C (27 mV), provides further evidence of the stabilizing effects of step-edges in GNF cavity and PtNP confinement within the GNF (Figure 2B and Table S1, Supporting Information). The poorer electrical connectivity of carbon black with the Pt gives rise to a higher electron transfer resistance and undesired increase in ORR overpotential as compared to the graphitic GNF.

The superior durability of PtNP@S-GNF becomes particularly striking over 50 000 cycles of ORR (Figure 3A,B and **Table 1**). While the initial specific activity of the commercial electrocatalyst Pt/C is better than the activity of our PtNP@S-GNF for an identical (total) Pt loading, beyond 10 000 cycles, the activity of Pt/C decreases dramatically due to a quick drop of the active surface area, with a loss of 71 % of the initial activity after 50 000 cycles (Figure 3A, and Figure S10, Supporting Information). Remarkably, under the same conditions the specific activity of PtNP@S-GNF material decreased only by 12% after 50 000 cycles showing a significantly more stable activity than that of Pt/C. It is worth noting that no significant change in the polarization curves of ORR was found for PtNP@S-GNF after durability tests (Figure 2B) confirming that the ORR mechanim remains unaltered throughout these extensive measurements. A Tafel analysis of the RRDE data (E vs $\log(J_k)$) for PtNP@S-GNF and the commercial catalyst after 50 000 potential cycles is shown in the Supporting Information (Figure S11, Supporting Information).

Detailed high resolution TEM imaging of the PtNP@S-GNF after 50 000 cycles revealed an unexpected transformation taking place inside GNF (Figure 1B,D, and Figures S12 and S13, Supporting Information). The rolled-up graphitic structure of internal step-edges in GNF become "unzipped" (Figure 1E) during the ORR forming a layer of amorphous carbon lining the inner surface of hollow GNF (Figure 1D). EDX analysis does not show any significant amount of oxygen in the amorphous material inside GNF, but it is apparent that PtNP adhere to the amorphous carbon presumably due to dangling bonds on the disordered carbon surface providing excellent anchoring sites for the catalytic centers (Figure 1G). While remaining confined within highly electrically conducting GNF and simultaneously being stabilized by the electrochemically generated amorphous carbon, remarkably, PtNP remain accessible to the reactants of ORR due to a gap of ≈10 nm between the layer of

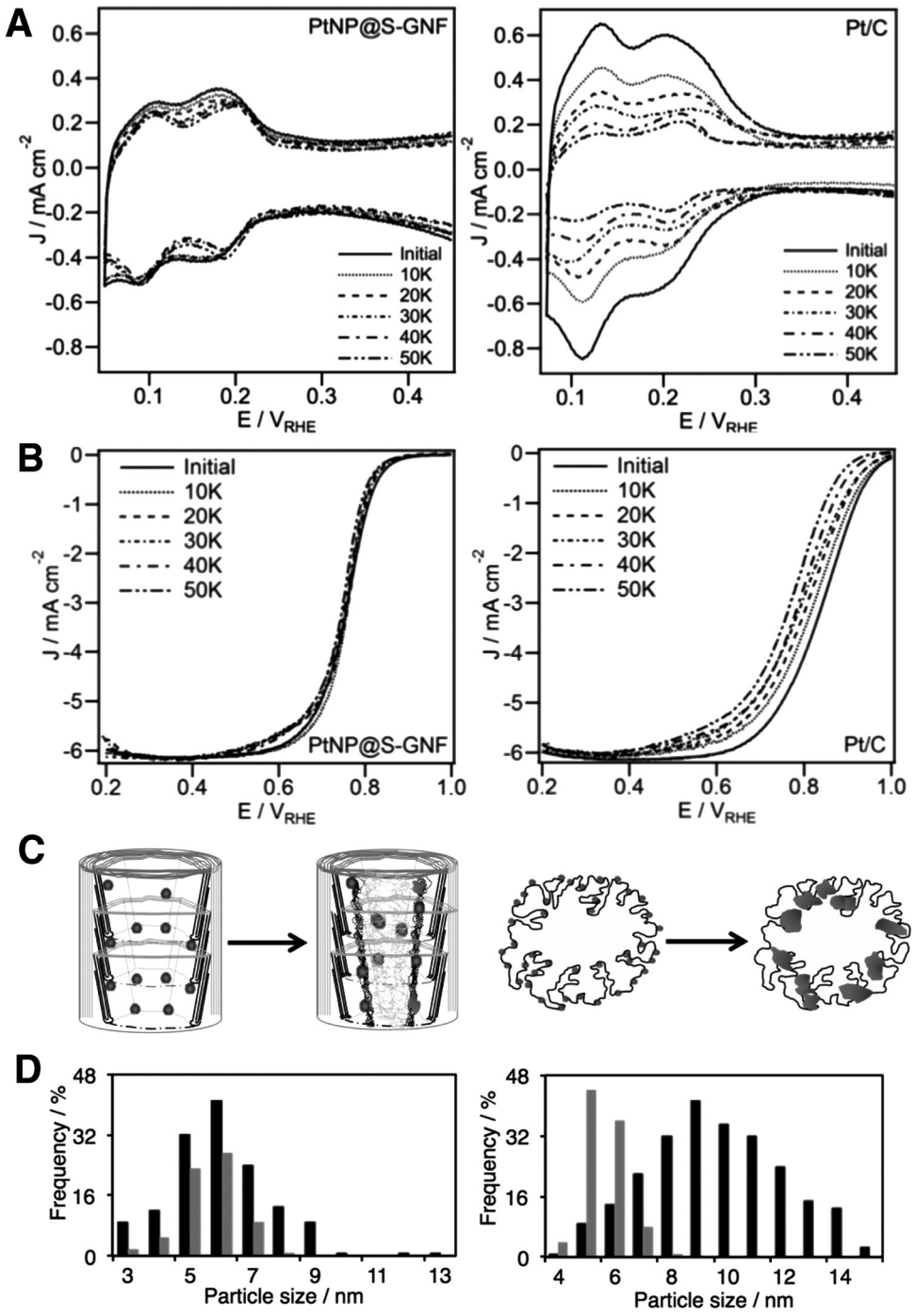

Figure 2. Comparison of the PtNP@S-GNF and Pt/C electrocatalysts over 50 000 potential cycles. A) voltammograms in the hydrogen adsorption/desorption potential region. B) ORR polarization curves, showing superior durability of PtNP@S-GNF. C) Schematic diagrams and D) nanoparticle size distribution before (grey data bars) and after (black data bars) 50 000 cycles of ORR, demonstrating a higher stability of catalytic nanoparticles to ripening in PtNP@S-GNF than in Pt/C which explains the significantly higher electrocatalytic durability of PtNP@S-GNF.

amorphous carbon and the GNF inner wall (Figure 1D, and Figures S12 and S13, Supporting Information), thus maintaining their high catalytic activity and exceptional durability even after 50 000 cycles due to the nanoscale confinement.

TEM images for PtNP@S-GNF after 50 000 cycles showed only a small change in PtNP size from 5.3 ± 0.4 nm to 6.2 ± 0.5 nm, unlike the significant increase in size for the commercial Pt/C from 3.4 ± 1.2 nm to 9.6 ± 2.5 nm found under the same conditions (Figure 2C,D). Comparison of the optical diffractograms of the encapsulated PtNPs before and after 50 000 cycles in TEM indicates no changes on the (110) lattice plane (*d*-spacing value of 0.193 nm) (Figure S14,

Adv. Mater. **2016**,
DOI: 10.1002/adma.201602485

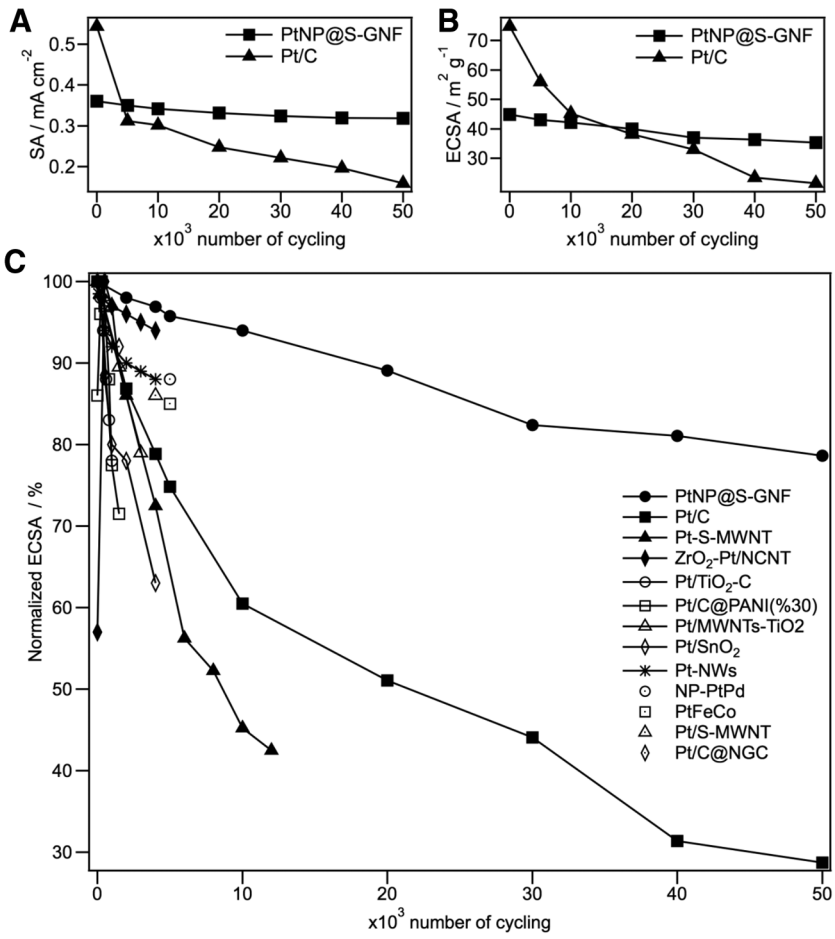

Figure 3. Comparison of PtNP@S-GNF and Pt/C over 50 000 potential cycles for A) the electrochemical active surface area (ECSA) and B) the specific activity (SA) at 0.85 V versus RHE. Comparison of changes of ECSA (%) for PtNP@S-GNF, Pt/C, and Pt electrocatalysts reported in the literature (Pt-S-MWCNT,[24] ZrO_2–Pt/NCNT,[19] Pt/TiO_2-C,[25] Pt/C@PANI(30%),[26] Pt/MWNTs-TiO_2,[27] Pt/SnO_2,[28] Pt-NWs,[29] NP-PtPd,[30] PtFeCo,[31] Pt/S-MWNT,[24] Pt/C@NGC[32]) emphasizing the overall excellent performance of PtNP@S-GNF (black circles) with respect to the state-of-the-art electrocatalysts.

Supporting Information) confirming that PtNP remain metallic state throughout the potential cycling.

A detailed comparison of the ECSA changes in potential cycling experiments for PtNP@S-GNF with other state-of-the-art Pt electroctalysts reported in the literature[19,24–32] (including the commercial Pt/C as a benchmark) (Figure 3C and Table S2, Supporting Information) further highligths the excellent long-term durability of PtNP within GNF retaining much of their activity over the 50 000 potential cycles thus outperforming all known electrocatalyst materials for ORR. The observed degradation in the half-wave potential of ORR polarization curves for PtNP@S-GNF of only 9 mV after 50 000 potential cycles is an exceptional behavior as shown by other studies.[33] These surprising and remarkable properties of PtNP@S-GNF open up a new strategy for harnessing the nanoscale confinement in sustainable use of platinum in electrocatalysis and other technological applications that require stabilization of metal NPs under harsh conditions. We believe that the reported synthetic strategy can be extended to other precious metals to inhibit their coalescence and thus to preserve their functional properties during potential cycling. Also the electrocatalysis in carbon nanoreactors can be extended to other processes of high technological value, such as methanol oxidation or hydrogen evolution reaction among others.

Experimental Section

1-octadecene (90%), oleylamine (>70%), oleic acid (90%), platinum (II) acetylacetonate, hexachloroplatinic acid ($H_2PtCl_6{\cdot}6H_2O$), ethylene glycol, nitric acid, isopropyl alcohol, hexane, and Nafion (5% solution in a mixture of lower aliphatic alcohols and water) were used as received from Sigma-Aldrich. GNF were supplied by Pyrograf Products Inc. and the Pt/C commercial catlayst (20 wt%, HiSPECTM 3000) was supplied by Johnson Matthey. Ultrapure water purified with Millipore Advantage A10 water equipment (resistivity 18.2 MΩ cm at 25 °C) was used in all experiments.

Shortened nanofibers (S-GNF): 50 mg of GNF as received with a length of 50–100 μm were mechanically ground in an ambient atmosphere using a Retsch MM 400 ball mill instrument, containing a steel ball with a diameter of 10 mm. The rolling speed of the milling machine is fixed at 10 Hz for 3 h to obtain the desired S-GNF (0.5–20 μm length).

Preparation of PtNP@S-GNF Hybrid Material: 10 mg of freshly heated S-GNF in air at 450 °C during 20 min were added under argon into a hexane suspension of PtNP obtained from platinum (II) acetylacetonate using a modified method previously reported in the literature by Wang et al.[23] with a 1:1 (PtNP:S-GNF) mass ratio. After stirring the mixture for 3 h, the hexane was gradually removed to concentrate the solution and finally dried. A small amount of hexane was then added to redissolve any nonencapsulated PtNP, and the mixture was stirred again for 3 h and dried. The process was repeated for three times to ensure

Table 1. Summary of electrochemical parameters for PtNP@S-GNF and Pt/C before and after 50 000 potential cycles.

	ECSA [$m^2\ g^{-1}$]	Theoretical surface area of NP [$m^2\ g^{-1}$]	Average NP size [nm]	Half-wave potential at 1600 rpm [V]	Specific activity at 0.85 V [mA cm^{-2}]	Mass activity at 0.85 V [A mg^{-1}]	Tafel slope @ RT LCD/HCD [mV dec^{-1}]
PtNP@S-GNF	44 ± 6	53 ± 4	5.3 ± 0.4	0.785	0.360	0.195	84/124
PtNP@S-GNF after	41 ± 5	42 ± 4	6.2 ± 0.5	0.776	0.318	0.181	86/138
Pt/C	74 ± 12	85 ± 15	3.3 ±0.7	0.840	0.544	0.396	95/136
Pt/C after	26 ± 3	60 ± 9	9.6 ± 2.5	0.792	0.159	0.096	105/145

that the majority of PtNP were transported inside S-GNF. The mixture was then sonicated in hexane (sonic probe diameter 3 mm, 20 kHz) for 30 min to remove nonencapsulated PtNPs, filtered through a PTFE membrane (pore size 0.45 μm) and washed with hexane, methanol, and finally acetone to yield a black solid product (8 mg).

Electrochemical Measurements: The electrochemical experiments were performed with an electrochemical work station CH instruments Inc. 700D using a glassy Carbon Electrode (GCE) and an Ag/AgCl electrode, as working electrode in a commercial (Pine Instruments) Pt ring-GCE disk electrode and reference electrode, respectively. The investigated samples were dropped onto the GCE as ink with an optimized constant platinum loading of 14 μg cm^{-2} and then dried in air.[34,35] CV was performed in nitrogen saturated 0.1 M $HClO_4$ at scan rates of 50 mV s^{-1} between 0.05 V and 1 V. Electrochemical durability test were carried out by continuously applying linear potential sweeps with a scan rate of 100 mV s^{-1} from 0.6 to 1.1 V for ORR in nitrogen saturated 0.1 M $HClO_4$. ECSA values in $m^2\ g_{Pt}^{-1}$ were calculated from the ECSA of platinum (A_{ec}), the platinum loading (W), and the geometric surface area of the electrode (A_{geo}) using the following expression: ECSA ($m^2\ g_{Pt}^{-1}$) = A_{ec} (m^2)/(W ($g_{Pt}\ m^{-2}$) × A_{geo} (m^2)). The ECSA of platinum (A_{ec}) was in turn calculated by dividing the total charge of the hydrogen desorption (QH_{des}) in μC by a known value for the amount of charge transferred during desorption of a monolayer of hydrogen from Pt (210×10^{-4} μC m^{-2}). The hydrogen desorption peak in the cyclic voltammogram is integrated to obtain the QH_{des} value.

Materials Characterization: XRD patterns were obtained on a Bruker AXS D8-Advanced diffractometer with Cu Kα radiation (λ = 1.5418 Å). TGA analyses were performed in air at a scan rate of 5 °C min^{-1} in a TA/TGA Q500 instrument. Samples for TEM analysis were prepared dispersing the material either in hexane or HPLC grade isopropanol by ultasonication, and then drop-casting the solution onto lacey carbon film coated copper grid. The samples were dried under nitrogen gas flow for 3 min to remove any residual solvent. HRTEM image was obtained on a JEOL 2010F TEM using accelerating voltage of 200 and 100 kV.

Supporting Information

Supporting Information is available from the Wiley Online Library or from the author.

Acknowledgements

This work was supported by the Royal Society (RG110291 and DH110080 for M.C.G), the Turkish government (PhD studentship for A.K.), the European Research Council (StG-277784 for A.N.K. and StG-679124 for M.C.G). The authors acknowledge the Nanoscale & Microscale Research Centre (NMRC) at the University of Nottingham for access to transmission electron microscopy facilities.

Received: May 10, 2016
Revised: July 28, 2016
Published online:

[1] D. L. Wang, C. V. Subban, H. S. Wang, E. Rus, F. J. DiSalvo, H. D. Abruna, *J. Am. Chem. Soc.* **2010**, *132*, 10218.
[2] N. V. Rees, R. G. Compton, *Energy Environ. Sci.* **2011**, *4*, 1255.
[3] T. Fujigaya, N. Nakashima, *Adv. Mater.* **2013**, *25*, 1666.
[4] Y. Y. Shao, G. P. Yin, Y. Z. Gao, *J. Power Sources* **2007**, *171*, 558.
[5] I. Dumitrescu, J. P. Edgeworth, P. R. Unwin, J. V. Macpherson, *Adv. Mater.* **2009**, *21*, 3105.
[6] Y. Shao, G. Yin, Z. Y. Gao, *Electrochim. Acta* **2006**, *51*, 5853.
[7] X. Wang, W. Li, Z. Chen, M. Waje, Y. Yan, *J. Power Sources* **2006**, *158*, 154.
[8] X. Zhou, J. Qiao, L. Yang, J. Zhang, *Adv. Energy Mater.* **2014**, *4*, 1301523.
[9] Y. Shao, G. Yin, J. Zhang, Y. Gao, *Electrochim. Acta* **2006**, *51*, 5853.
[10] X. Wang, W. Li, Z. Chen, M. Waje, Y. Yan, *J. Power Sources* **2006**, *158*, 154.
[11] X. Wang, M. Waje, Y. Yan, *Electrochem. Solid-State Lett.* **2005**, *8*, A42.
[12] A. C. C. Tseung, K. Y. Chen, *Catal. Today* **1997**, *38*, 439.
[13] X. Cui, J. Shi, H. chen, L. Zhang, L. Guo, J. Gao, J. Li, *J. Phys. Chem. B* **2008**, *112*, 12024.
[14] H. Chhina, S. Campbell, O. Kesler, *J. Electrochem. Soc.* **2007**, *154*, B533.
[15] R. Ganesan, D. J. Ham, J. S. Lee, *Electrochem. Commun.* **2007**, *9*, 2576.
[16] K.-S. Lee, I.-S. Park, Y.-H. Cho, D.-S. Jung, N. Jung, H.-Y. Park, Y.-E. Sung, *J. Catal.* **2008**, *258*, 143.
[17] A. L. Santos, D. Profeti, P. Olivi, *Elctrochim. Acta* **2005**, *50*, 2615.
[18] H. L. Pang, X. H. Zhang, X. X. Zhong, B. Liu, X. G. Wei, Y. F. Kuang, J. H. Chen, *J. Colloid Interface Sci.* **2008**, *319*, 193.
[19] N. Cheng, M. N. Banis, J. Liu, A. Riese, X. Li, R. Li, S. Ye, S. Knights, X. Sun, *Adv. Mater.* **2015**, *27*, 277.
[20] M. C. Gimenez-Lopez, A. La Torre, M. W. Fay, P. D. Brown, A. N. Khlobystov, *Angew. Chem. Int. Ed.* **2013**, *52*, 2051.
[21] A. La Torre, M. C. Gimenez-Lopez, M. W. Fay, G. A. Rance, W. A. Solomonsz, T. W. Chamberlain, P. D. Brown, A. N. Khlobystov, *ACS Nano* **2012**, *6*, 2000.
[22] A. La Torre, M. C. Gimenez-Lopez, M. W. Fay, C. H. Lucas, P. D. Brown, A. N. Khlobystov, *Small* **2015**, *11*, 2756.
[23] C. Wang, H. Daimon, S. Sun, *Nano Lett.* **2009**, *9*, 1493.
[24] T. J. Kim, G. Kwon, Y. T. Kim, *Chem. Commun.* **2014**, *50*, 596.
[25] Z.-Z. Jiang, Z.-B. Wang, Y.-Y. Chu, D.-M. Gu, G.-P. Yin, *Energy Environ. Sci.* **2011**, *4*, 728.
[26] S. Chen, Z. Wei, X. Qi, L. Dong, Y.-G. Guo, L. Wan, Z. Shao, L. Li, *J. Am. Chem. Soc.* **2012**, *134*, 13252.
[27] Z.-Z. Jiang, Z.-B. Wang, Y.-Y. Chu, D.-M. Gu, G.-P. Yin, *Energy Environ. Sci.* **2011**, *4*, 2558.
[28] M. Dou, M. Hou, D. Liang, W. Lu, Z. Shao, B. Yi, *Electrochim. Acta* **2013**, *92*, 468.
[29] M. A. Hoque, F. M. Hassan, D. Higgins, J. Y. Choi, M. Pritzker, S. Knights, S. Ye, Z. Chen, *Adv. Mater.* **2015**, *27*, 1134.
[30] H. Duan, C. Xu, *Electrochim. Acta* **2015**, *152*, 417.
[31] B. Arumugam, B. A. Kakade, T. Tamaki, M. Arao, H. Imai, T. Yamaguchi, *RSC Adv.* **2014**, *4*, 27510.
[32] Y. Nie, S. Chen, W. Ding, X. Xie, Y. Zhang, Z. Wei, *Chem. Commun.* **2014**, *50*, 15431.
[33] J. Zhang, K. Sasaki, E. Sutter, R. R. Adzic, *Science* **2007**, *315*, 220.
[34] M. T. M. Koper, *Fuel Cell Catalysis: A Surface Science Approach*, John Wiley & Sons, Hoboken, NJ, USA **2009**.
[35] D. E. Ramaker, A. Korovina, V. Croze, J. Melke, C. Roth, *Phys. Chem. Chem. Phys.* **2014**, *16*, 13645.

ADVANCED MATERIALS

Supporting Information

for *Adv. Mater.*, DOI: 10.1002/adma.201602485

Extremely Stable Platinum-Amorphous Carbon Electrocatalyst within Hollow Graphitized Carbon Nanofibers for the Oxygen Reduction Reaction

Maria del Carmen Gimenez-Lopez, Abdullah Kurtoglu, Darren A. Walsh, and Andrei N. Khlobystov**

Supporting Information

Extremely Stable Platinum-Amorphous Carbon Electrocatalyst Formed within Hollow Graphitised Carbon Nanofibers during Oxygen Reduction Reaction

Maria del Carmen Gimenez-Lopez[1*], *Abdullah Kurtoglu,*[1] *Darren Walsh,*[1] *and Andrei N. Khlobystov.*[1,2*]

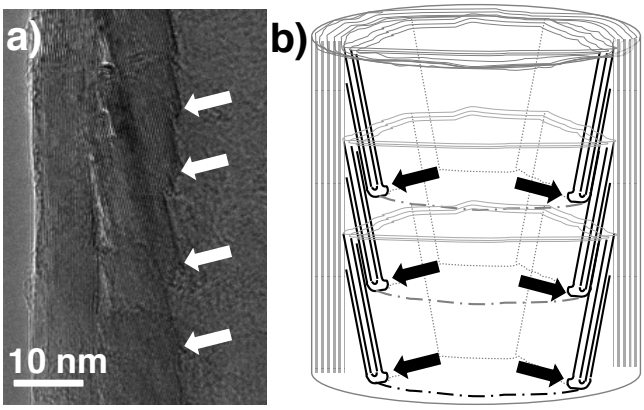

Figure S1. HRTEM image (a) and schematic representation of the herringbone GNF step-edges (b).

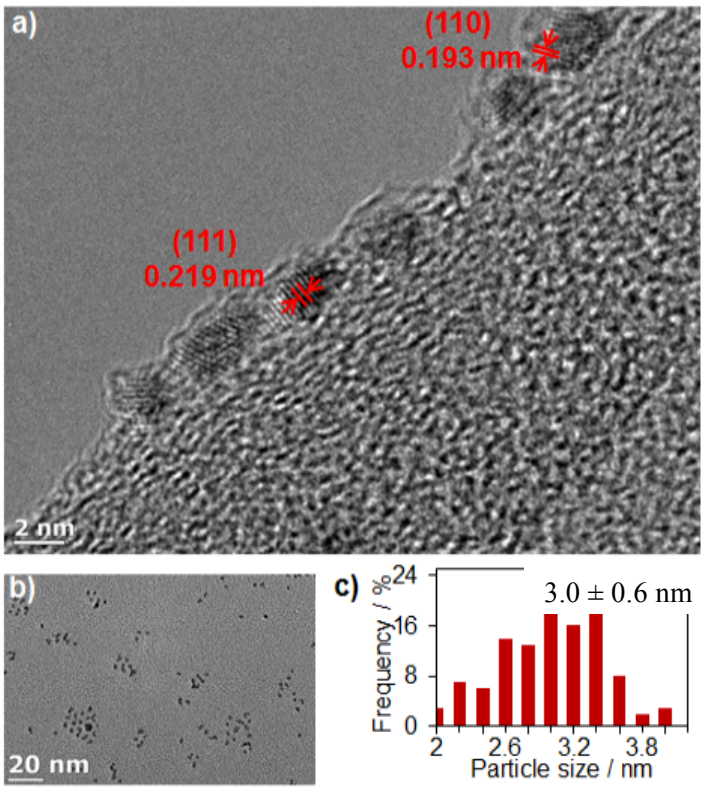

Figure S2. HRTEM images of PtNP dispersed on the carbon film (**a-b**) and the particle size distribution and average size of the preformed PtNP (**c**).

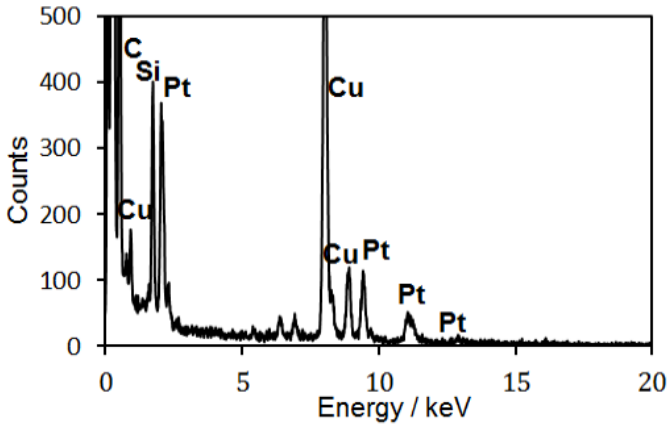

Figure S3. Energy-dispersive X-ray (EDX) analysis of PtNP onto copper-grid mounted "lacey" carbon film.

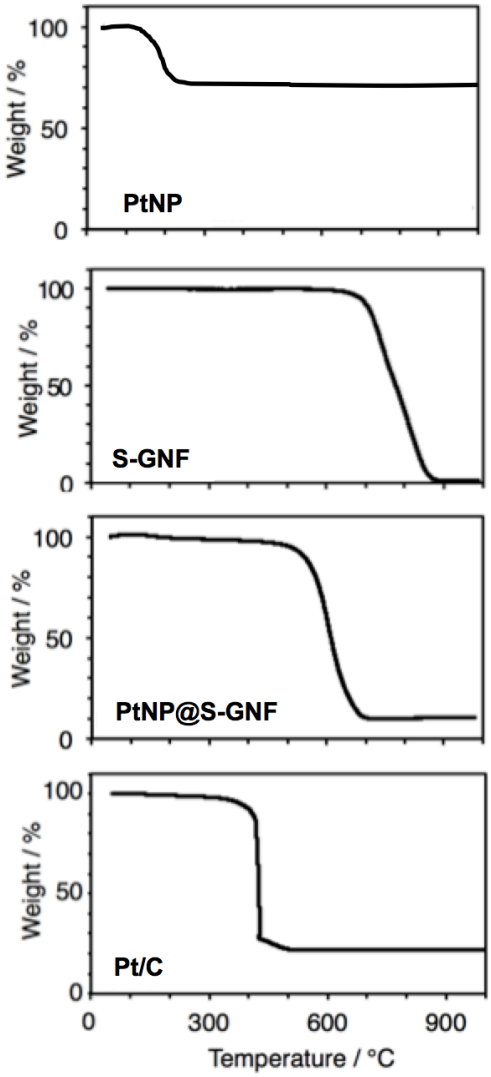

Figure S4. Thermal gravimetric analysis (TGA) carried out in air up to 1000 ˚C with a scan rate of 5˚C/min for PtNP, S-GNF, PtNP@S-GNF and Pt/C.

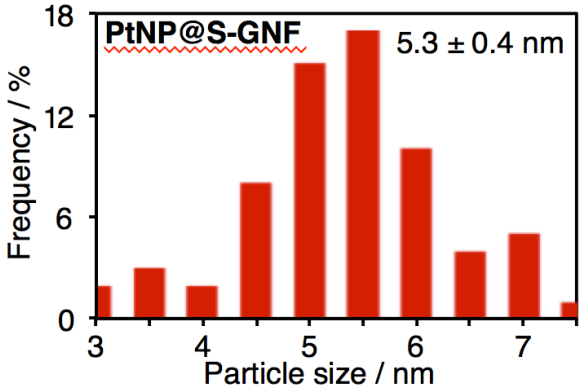

Figure S5. Particle size distribution and average sizes for PtNP inside S-GNF (PtNP@S-GNF) after heating in air at 175 ˚C for 2 h.

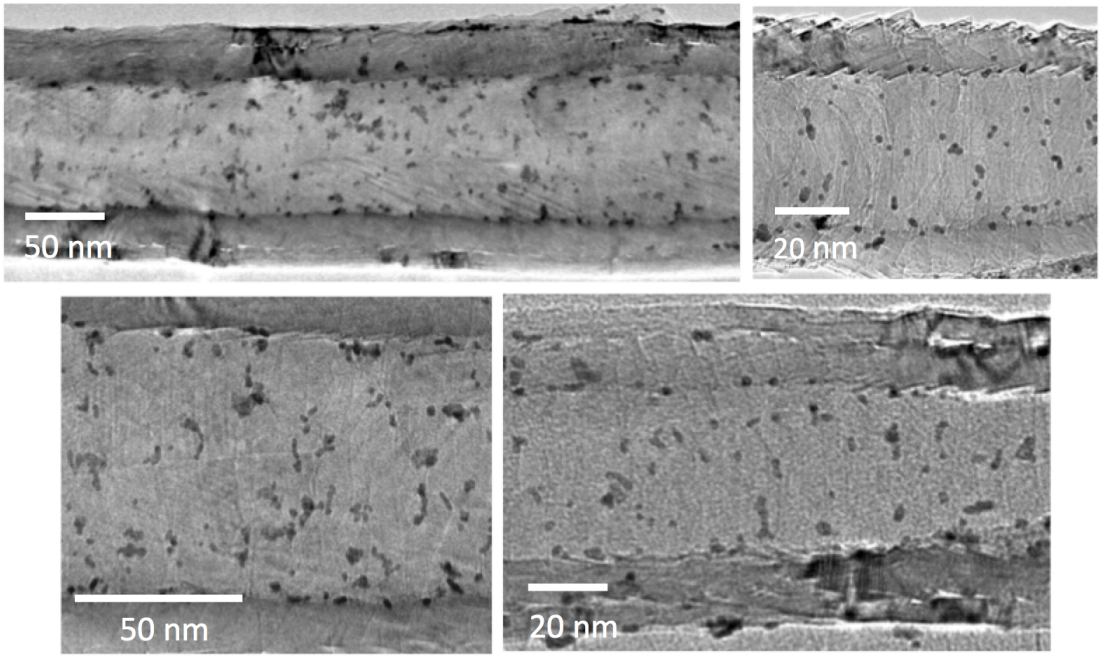

Figure S6. HRTEM images of PtNP@S-GNF before potential cycling.

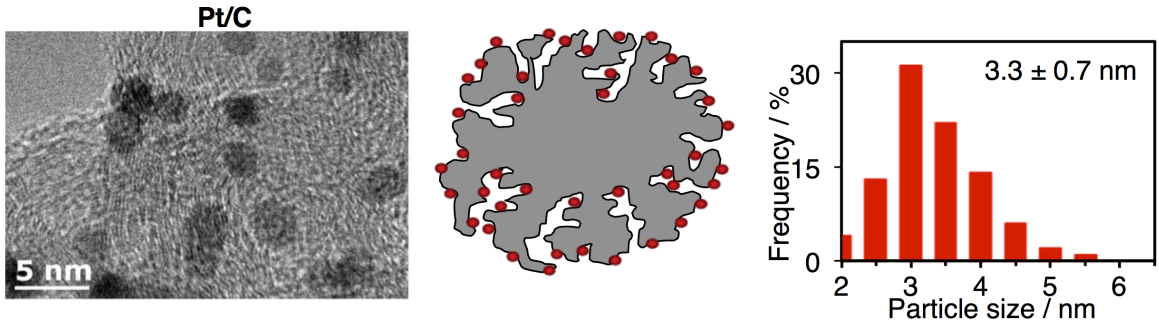

Figure S7. HRTEM images, schematic diagrams, particle size distributions and average size of Pt nanoparticles for the standard commercial electrocatalyst Pt/C (Johnson Matthey 20 wt%, HiSPECTM3000).

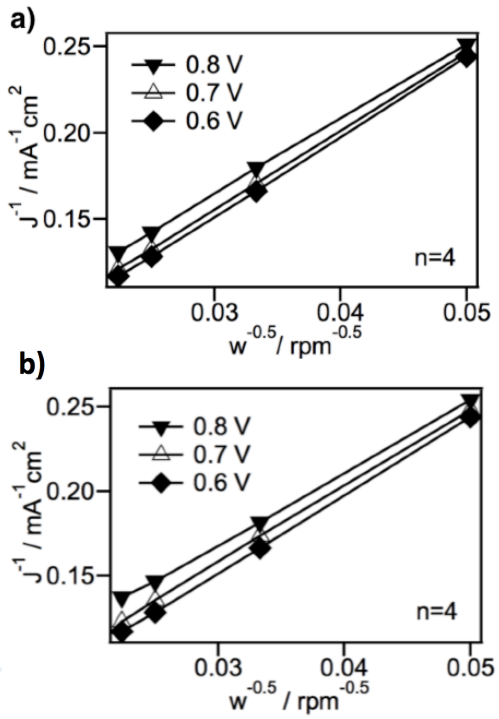

Figure S8. Koutecky-Levich plots of J^{1} (current density) *versus* $\omega^{-0.5}$ (rotating speed) at various potentials extracted from the data I-V curves, current densities (J) normalized to the geometric electrode area for PtNP@S-GNF (a) and Pt/C (b).

Table S1. Summary of electrochemical parameters for PtNP@S-GNF and Pt/C before and after 5,000 potential cycles.

	ECSA (m^2/g)	Theoretical surface area of NP	Average NP size (nm)	Half-wave potential at 1600 rpm (V)	Specific activity at 0.85 V (mA/cm^2)	Mass Activity at 0.85 V (A/mg)	Tafel slope @ RT lcd/hcd (mV/dec)
PtNP@S-GNF	44 ± 6	53 ± 4	5.3 ± 0.4	0.785	0.36	0.195	84/124
PtNP@S-GNF after	43 ± 5	42 ± 4	5.8 ± 0.5	0.783	0.35	0.190	84/136
Pt/C	74 ± 12	85 ± 15	3.3 ±0.7	0.840	0.544	0.396	95/136
Pt/C after	56 ± 8	60 ± 9	4.7 ± 0.8	0.813	0.312	0.182	75/131

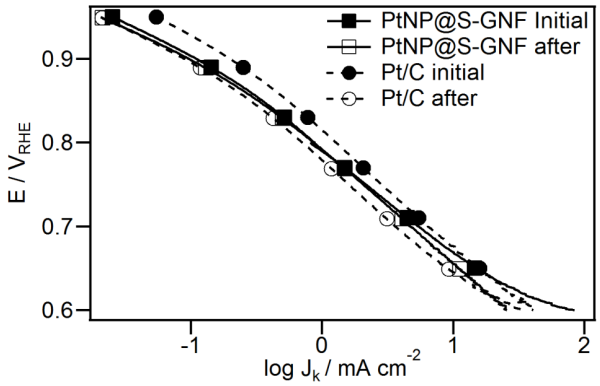

Figure S9. Tafel plots for the ORR normalised to the real surface area at room temperature, (anodic sweep 5 mV/s, 1600 rpm) on PtNP@S-GNF and Pt/C before and after 5,000 cycles of ORR.

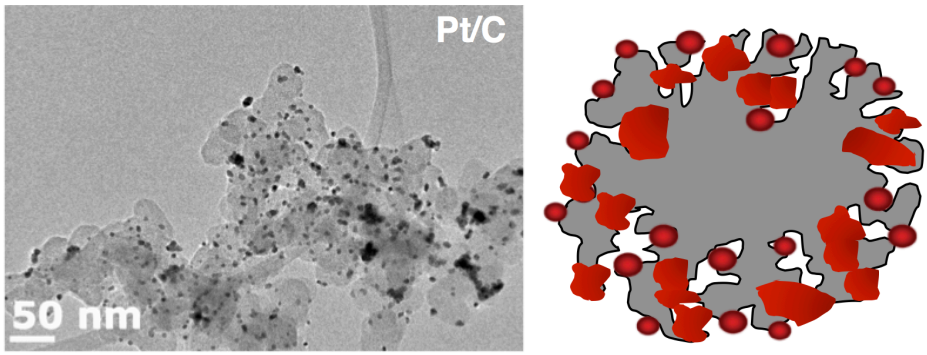

Figure S10. HRTEM images and schematic diagram for the Pt/C commercial catalyst after 50,000 cycles of ORR.

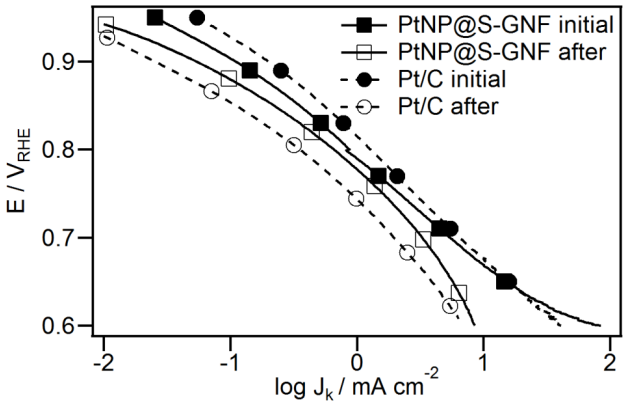

Figure S11. Tafel plots for the ORR normalised to the real surface area at room temperature, (anodic sweep 5 mV/s, 1600 rpm) on PtNP@S-GNF and Pt/C before and after 50,000 cycles of ORR.

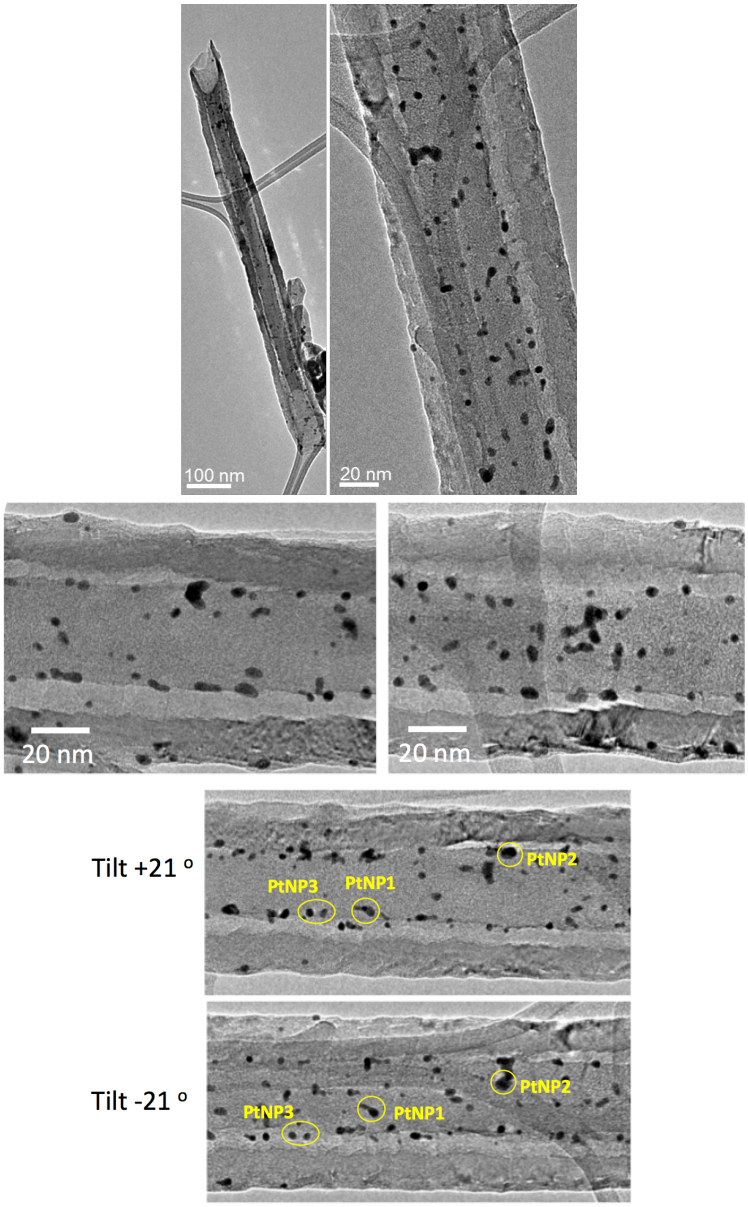

Figure S12. HRTEM images of the PtNP@S-GNF after 50,000 potential cycling. When tilted around GNF axis the PtNPs change their positions (as illustrated for three examples highlighted in circles) but remain inside GNF and adhered primarily on the layer of amorphous carbon rather than the GNF inner wall.

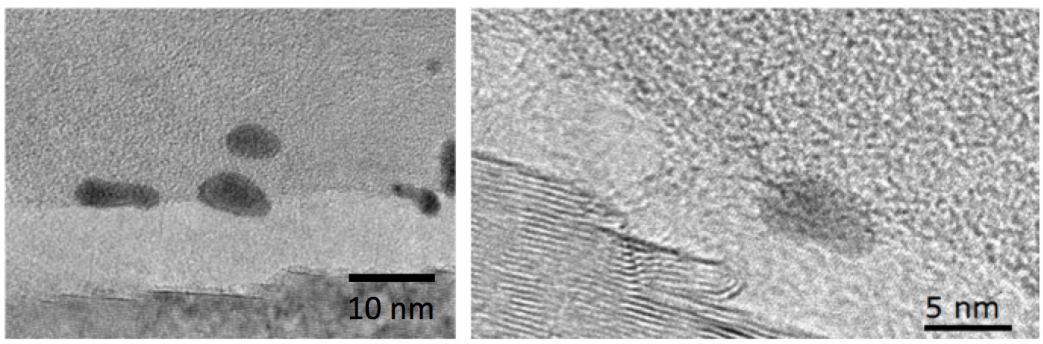

Figure S13. High-magnification HRTEM images of PtNP in PtNP@S-GNF after 50,000 potential cycling.

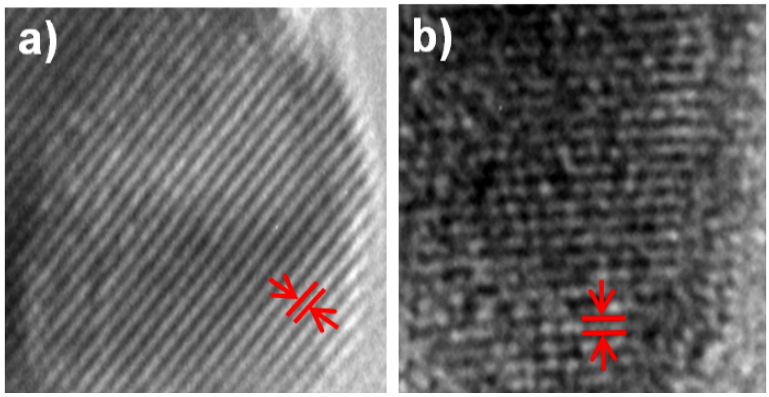

Figure S14. HRTEM images showing lattice planes correlating (110) d-spacing value of 0.193 nm of PtNP on step-edges before (a) and after (b) 50K potential cycling for lifetime stability experiments.

Table S2. Summary of electrochemical parameters for different platinum electrocatalyst from literature, our PtNP@S-GNF electrocatalyst and Pt/C commercial catalyst. (*this work, § I_{sa} at 0.85 V, $^{\#}$ I_{mass} at 0.9 V, $^{¥}$ I_{sa} at 0.9 V)

Sample name	Conditions	% ECSA Loss (m^2/g)	% Average NP size increase (nm)	% Half-wave potential at 1600 rpm (V)	% Activity loss	Cycling number
PtNP@S-GNF*	0.6-1.1 V vs. RHE, 0.1M $HClO_4$, 100 mV/s, O_2, RT	22	17	9	19§	50K
Pt/C*	0.6-1.1 V vs. RHE, 0.1M $HClO_4$, 100 mV/s, O_2, RT	72	190	48	79§	50K
Pt–S-MWNT[1]	0.395-0.895 V vs. Ag/AgCl, 0.1M $HClO_4$, 50 mV/s, 100 rpm, O_2	57.5	-	5	-	12K
PFSA-Pt/CNTs[2]	0.6 and 1.2 V vs. RHE, 50 mV/s , 0.1 M $HClO_4$, N2	-	45	-	-	3K
NP-PtPd[3]	0.6 -1.0 V vs. RHE, 0.1 M $HClO_4$	12	-	9	-	5K
PtFeCo[4]	Applying square wave potential cycling, at 0.6 V for 3s and 1.0 V for 3s vs. RHE, 0.1 M $HClO_4$	15	17.5	13	21.5$^{\#}$	5K
Pt/S-MWNT[5]	0.6-1.1 V vs. RHE, 0.1 M $HClO_4$, 50 mV/s, O_2	14	-	1	18$^{¥}$	4K
N-Pt_3Fe_1/C[6]	0.6 -1.2 V vs. NHE, 0.1 M $HClO_4$, O_2	-	-	-	7$^{¥}$	20K
ZrO_2 -Pt/NCNT 600˚C[7]	0.6 -1.2 V vs. RHE, 0.5 M H_2SO_4,50 mV/s,O_2,	8	0	-	3.5$^{\#}$	4K
Pt/C@NGC[8]	0-1.2 V vs. RHE, 0.1 M HClO4,50 mV/s, N2	8	15	16	-	1.5 K
Carbon riveted Pt/TiO_2-C[9]	-------	21.5	-	-	-	1K
Pt/C@PANI(30%)[10]	0-1.2 V vs. RHE, 0.5 M H_2SO_4, 50 mV/s, N_2 RT	30	71	-	-	1.5K
Carbon riveted microcapsule Pt/MWCNTs-TiO_2[11]	-------	12				3K
Pt/SnO_2[12]	-------	36				4K
Pt-NWs[13]	0.6-1.2 V vs. RHE, 0.5M H_2SO_4,50 mV/s, O_2	13	-	9	-	4K

References:

[1] T. J. Kim, G. Kwon, Y. T. Kim, *Chemical Communications* **2014**, *50*, 596-598.

[2] E. Negro, M. A. De Vries, R. Latsuzbaia, G. J. M. Koper, *Fuel Cells* **2014**, *14*, 350-356.

[3] H. Duan, C. Xu, *Electrochimica Acta* **2015**, *152*, 417-424.

[4] B. Arumugam, B. A. Kakade, T. Tamaki, M. Arao, H. Imai, T. Yamaguchi, *RSC Advances* **2014**, *4*, 27510-27517.

[5] S.-A. Park, D.-S. Kim, T.-J. Kim, Y.-T. Kim, *ACS Catalysis* **2013**, *3*, 3067-3074.

[6] X. Li, L. An, X. Chen, N. Zhang, D. Xia, W. Huang, W. Chu, Z. Wu, *Scientific Reports* **2013**, 3:3234.

[7] N. Cheng, M. N. Banis, J. Liu, A. Riese, X. Li, R. Li, S. Ye, S. Knights, X. Sun, *Advanced Materials* **2015**, *27*, 277-281.

[8] Y. Nie, S. Chen, W. Ding, X. Xie, Y. Zhang, Z. Wei, *Chemical Communications* **2014**, *50*, 15431-15434.

[9] Z.-Z. Jiang, Z.-B. Wang, Y.-Y. Chu, D.-M. Gu, G.-P. Yin, *Energy Environmental Science* **2011**, *4*, 728-735.

[10] S. Chen, Z. Wei, X. Qi, L. Dong, Y.-G. Guo, L. Wan, Z. Shao, L. Li, *Journal of the American Chemical Society* **2012**, *134*, 13252-13255.

[11] Z.-Z. Jiang, Z.-B. Wang, Y.-Y. Chu, D.-M. Gu, G.-P. Yin, *Energy Environmental Science* **2011**, *4*, 2558-2566.

[12] M. Dou, M. Hou, D. Liang, W. Lu, Z. Shao, B. Yi, *Electrochimica Acta* **2013**, *92*, 468-473.

[13] S. Sun, G. Zhang, D. Geng, Y. Chen, R. Li, M. Cai, X. Sun, *Angewandte Chemie International Edition* **2011**, *50*, 422-426.